Kinetic control of surface patterning by laser-induced photochemical deposition in liquid solutions. II. Experimental investigations

Emmanuel Hugonnot, Alexandru Popescu, Sylvie Hanifi-Kadi, and Jean-Pierre Delville*
Centre de Physique Moléculaire Optique et Hertzienne, UMR CNRS/Université No.5798, Université Bordeaux I, 351 Cours de la Libération, F-33405 Talence Cedex, France
(Received 2 December 2003; revised manuscript received 7 February 2004; published 27 May 2004)

We experimentally analyze the real-time formation of periodic surface patterning resulting from laser-driven photochemical deposition in liquid solutions. Using photochemical deposition of chromium hydroxide layers driven by a continuous Ar^+ laser wave in a potassium chromate solution, we analyze the kinetic formation of three different types of patterning: dot array, periodic line writing, and holographic grating formed by interfering beams. Results are also presented for both flat and curved substrates. In each case, the deposit growth laws are measured and they show the emergence of scaling regimes that are predicted by our model [E. Hugonnot and J. P. Delville, Phys. Rev. E **69**, 051605 (2004)]. Data taken from literature are also confronted to the model. The observed agreement suggests that a unified picture of the processes involved for photodeposition driven by a one-photon absorption can be devised, whatever the initial photosensitive medium is. This kinetic control of photodeposition, associated to the versatility in monitoring the geometry of laser/medium interaction and the flexibility in deposited materials by various photochemical reactions, offers a valuable level of development in substrate patterning for lithographic or holographic applications.

DOI: 10.1103/PhysRevE.69.051606 PACS number(s): 81.15.Fg, 81.10.Dn, 42.40.Eq, 42.70.Gi

I. INTRODUCTION

Laser-writing technologies become the corner stone of numerous emerging technologies in material processing [1], because the desired structures are built *in situ* in one step, while lithographic techniques derived from microelectronics, are usually based on a multiple mask process involving different stages. The resulting rapid prototyping makes laser direct writing very appealing and challenging in a wide range of applications. For example, microelectronic components [2] and interconnects [3] are successfully realized by laser writing of numerous materials. The main advantages of laser-beam writing are the small lateral features, of the order of microns, that can be achieved with simultaneous control of the depth structure. Moreover, laser pencils create near-continuous and smooth profiles rather than stepped structures generated with masks. These aspects are thus very appealing in micro-optical applications that use beam splitters and shapers, diffractive microelements, or microlens array for telecom and datacom.

Among the different laser-writing techniques (photoelectrochemical etching [4], photodoping [5], laser ablation [6], laser machining [7], photo-diagnostics [8], chemical processing with lasers [9], for instance), photodeposition of thin films from liquid solution [10] is very attractive because light excitation is generally efficient and experiments are easy to manage. Indeed, the writing beam is injected through an optical window into a cell that contains a photoactive solution. Photons are absorbed and trigger a photochemical reaction to produce a new species. Above some onset in concentration, classically the solubility of this new species, nucleation occurs and solid nanoparticles are deposited on the internal face of the entrance window. Then, these particles grow, coalesce, and form a continuous film in the illuminated area [11]. Consequently, by illumination with a spatially well-defined laser excitation, various dots, lines, or more intricate patterns can be directly deposited in a single step on a solid substrate in contact with the photoactive solution. While this writing procedure is very easy to implement, the optimization of the induced patterns requires a perfect tailoring of the material deposited because the performances of the final devices strongly depend on the size, shape, and distribution of these deposits. That is why we develop in a companion paper [12] (referred to from now on as Part I) a thermodynamic description of the kinetics of deposition under exposition to a continuous laser wave.

Considering a reaction/diffusion scheme involving the one-photon excitation of a two-level system, we analyzed the thermodynamic behavior of the field variation of the photoreaction product, and deduced the coarsening of the resulting deposit in presence of the light intensity distribution. Beyond predictions on radial and axial growth, our main goal was to describe how the kinetics of photodeposition can be efficiently used to build holographic gratings and tailor their optical phase and amplitude properties. We focused our attention to dot and line arrays created by a serial procedure, and periodic structures produced by the interference field of two exciting beams (parallel procedure). Moreover, to present a universal description of the involved processes, we extended coarsening theories of phase transitions [13] and demonstrate scaling behaviors in photodeposition driven by diffusion and solute adsorption. While such an approach is usually presented in a fundamental context, it has also important drawbacks toward very practical situations because a unified view of photodeposition is presented, whatever the photosensitive mixture used is.

The present study is devoted to an experimental investigation of these predictions. We experimentally analyze the

*Email address: jp.delville@cpmoh.u-bordeaux1.fr

kinetics of surface patterning by the photochemical deposition of chromium hydroxide layers driven by a continuous Ar^+ laser wave in a potassium chromate solution. Results are confronted to the model developed in Part I. We also consider the three procedures mentioned above to build periodic patterns, i.e., dot and line array, and periodic modulation deposited by interfering beams, and analyze in each case the deposit growth as a function of the exciting parameters.

The paper is organized as follows. We present in Sec. II, the medium we choose for the investigation, its properties, and the general aspects of the experimental scheme. The mechanisms at the origin of the photochemical production of a new species from the photosensitive mixture are discussed and we illustrate how this production can easily lead to photodeposition when concentration reaches solubility. Then, the radial growth of a circular deposit is described in Sec. III. We show that growth laws are monitored by the competition between two length scales: the beam waist and the attenuation length within the medium due to light absorption. By defining a rescaled optical absorption W using these two quantities, we analyze photodeposit growth in the two opposite regimes $W \gg 1$ and $W \ll 1$, as well as for the crossover in W. In the two first cases, we find scaling laws that are in agreement with expectations. Scaling is also investigated for deposition on both flat and curved substrates. Moreover, we show in each case how the observed behaviors can be used to build periodic patterns. We also analyze the late stage growth of the deposit thickness using data published in the literature. Section IV is devoted to line writing by extending the previous results to optical excitation by a scanning beam. We particularly explore the influence of the scanning velocity on the transverse line growth under illumination. Using the same formalism, Sec. V is entirely devoted to the growth of surface relief gratings monitored by two interfering pump beams. We show that the analysis of the temporal behavior of the diffraction pattern of a probe beam is particularly efficient to retrieve the thickness dynamics of the induced deposit. We finally conclude in Sec. VI. Considering the good agreement observed between theory and experiments, the present investigation offers the opportunity to show that photodeposited patterns can be confidently devised when driven by a one-photon photochemical reaction.

II. THE PHOTOACTIVE MEDIUM AND ITS OPTICAL EXCITATION

Experiments are performed at room temperature in an acidic liquid mixture composed of potassium chromate, ethanol, hydrochloric acid, and water. This choice is motivated by the well-known photoreduction of Cr(VI) ions into Cr(III) ones used for hologram recording in dichromated gelatins [14]. The mass composition of our sample is: potassium chromate K_2CrO_4 (10 wt %), ethanol (8 wt %), 10N hydrochloric acid HCl (10 wt %) and ultrapure water (72 wt %). It is chosen to be below the solubility threshold. The stability of the solution was probed by absorption spectra during a one month period; no variation was detected. The mixture is prepared according to the following procedure. In a first step, potassium chromate, ethanol, and pure water are mixed together. The pH of the solution is then adjusted by adding hydrochloric acid. Indeed, different form of Cr(VI) ions exist in aqueous solutions, either $HCrO_4^-$ or CrO_4^{2-}, according to the acid-base equilibrium $HCrO_4^- \rightleftharpoons CrO_4^{2-} + H^+$ (pK=6.49) [15]. We worked at pH=3 in order to have $HCrO_4^-$ as the major species in the solution, since it corresponds to the hexavalent form of chromium that is activated by light in the blue-green wavelength range of a continuous Ar^+ laser. An organic compound, here an alcohol (ROH), is also necessary to enhance the photoreduction of $HCrO_4^-$ to a Cr(III) product. The composition of the mixture has also been chosen to obtain a photoproduced Cr(III) species of low solubility in order to increase the photodeposition yield. X-ray photoelectron spectroscopy and low angle x-ray diffraction show that photodeposited films of Cr(III) are mainly constituted by amorphous $Cr(OH)_3$ [16], as expected from the classical formation of chromate conversion coatings [17]. On the other hand, it is now well established that the major pathway from the Cr(VI) to the Cr(III) form starts from a light-induced excitation of Cr(VI) followed by a reduction to a Cr(V) intermediate and a dark reaction from Cr(V) to Cr(III) [14]. One has

$$\mathrm{Cr(VI)} + h\nu \rightleftharpoons \mathrm{Cr(VI)}^*,$$

$$\mathrm{Cr(VI)}^* + R\mathrm{OH} \rightarrow \text{“ Cr(V) ”} \rightarrow \cdots \rightarrow \mathrm{Cr(III)}, \qquad (1)$$

where $h\nu$ represents the energy of the absorbed photon.

The photochemical reaction is driven by a linearly polarized TEM_{00} Ar^+ laser (wavelength in vacuum: $\lambda_0 = 5145$ Å). In a single wave excitation, the beam intensity along the propagation axis z is written as $I(r,z) = P/(\pi a_0^2)\exp(-r^2/a_0^2)\exp(-\sigma z)$ in cylindrical coordinates (r,z), where P, a_0, and σ are, respectively, the incident power, the beam radius, and the absorption of the initial liquid mixture. We treat here the beam width a_0 as constant because experiments in resonant liquids require thin samples, and the wave symmetry can be considered as almost cylindrical around the propagation axis for axial distances $z \leqslant z_d = 2\pi n a_0^2/\lambda_0$ from the beam-waist location, where n is the index of refraction of the liquid mixture. The mixture is enclosed in a homemade tight cell composed of a glass slide and a cover slip separated by 30 or 100 μm thick Mylar spacers to prevent disturbing thermal overheating resulting from light absorption at the wavelength used. The cover slip is also silanized to avoid any photochemical deposition on both cell windows. With $\sigma = 1.3 \times 10^4$ m^{-1} and a thermal conductivity $\Lambda_{th} \approx 1$ W K^{-1} m^{-1}, the temperature rise induced by the beam (Sec. III A in Part I) is typically $\Delta T \simeq 30$ K for $P = 30$ mW and $a_0 = 150$ μm (i.e., for the largest ratio P/a_0 used in the present study). Boiling and convection are then prevented. Moreover, we did not see any variation of the precipitation onset of the Cr(III) species produced because its solubility is almost constant over a wide range in temperature around the room temperature for the concentration investigated [18]. Consequently, thermal couplings do not affect noticeably the photochemical deposition described in the present work, and can be discarded.

According to Eq. (1), the production in Cr(III) increases versus optical excitation. As soon as its solubility is locally reached within the illuminated area, photoprecipitation of Cr(III) occurs. As already discussed in a series of studies on amorphous selenium film deposition [19], a rather complex dynamics is observed. Three main regimes are generally expected. At short time, spheroids are heterogeneously nucleated on the substrate and grow independently. In a second stage, aggregation between growing spheroids, followed by internal restructuring inside the whole structure, leads to the formation of a porous layer of increasing compactness. Reorganization is still present during the late-stage growth of a photodeposit, but growth mainly occurs by the irreversible adsorption of the diffusing particles photoproduced, here Cr(III) molecules. In the following, we essentially focus our experimental investigation onto this late stage when the deposit is compact and large compared to any molecular length scale involved in the process. Some digressions on the two other regimes will be nevertheless presented to illustrate how these regimes can strongly influence the late-stage growth in some special situations.

III. GROWTH OF CIRCULAR PHOTODEPOSITS

A. Theoretical background

In this section, we briefly summarize the main stages in the derivation of the deposit growth rate for circular photodeposits driven by a one-photon photochemical reaction (Sec. III of Part I). According to Eq. (1), one can assume that production in Cr(III) is driven by a reaction-diffusion process involving a one-photon photochemical reaction. Within this framework, the reaction scheme is reduced to its two main steps:

$$A + h\nu \underset{k_\downarrow}{\overset{k_\uparrow}{\rightleftharpoons}} A^*[\mathrm{Cr(VI)}\textit{excitation/relaxation}],$$

$$A^* + B \overset{k_{A^*B}}{\rightleftharpoons} C[\mathrm{Cr(III)}\textit{production/decomposition}], \qquad (2)$$

where A, A^*, B, and C are, respectively, Cr(VI), excited Cr(VI), ethanol, and Cr(III) species and $k_\uparrow$, $k_\downarrow$, and k_{A^*B} are the reaction rates associated to the different processes. Assuming that the kinetics of excitation/relaxation of Cr(VI) is much faster than any mass diffusion involved in the dynamics of photoprecipitation, the volume fractions Φ_A and Φ_{A^*}, respectively, in Cr(VI) and Cr(VI)* are estimated at steady state, and are simply related by $\Phi_{A^*}=(k_\uparrow/k_\downarrow)\Phi_A$. We consider a one-photon electronic transition to calculate the ratio $k_\uparrow/k_\downarrow$, and use the standard Einstein coefficients for the one-photon absorption and the spontaneous and stimulated emissions. For a pump intensity I smaller than the saturation intensity I_S for the one-photo transition, the concentration Φ_C in Cr(III) is described by a field-modified reaction-diffusion equation:

$$\frac{\partial \Phi_C(r,z,t)}{\partial t} = D_C \nabla^2 \Phi_C(r,z,t) + K^* I(r,z), \qquad (3)$$

where D_C is the mass diffusion constant of the product Cr(III) and K^* is the normalized reaction rate for the Cr(VI)$^* \rightarrow$ Cr(III) reaction; it can be noticed that $K^* \propto \sigma$. Moreover, since the measured deposit is incomparably larger than any molecular size involved in the process, we assimilate its shape to a spherical cap of height h on beam axis and radius R_d on the substrate, and build a "droplet growth" model driven by the diffusion and the adsorption of Cr(III) molecules produced in the illuminated area. The radial growth rate is then obtained by equating the flux in Cr(III) at the surface of the deposit with its volume variation. As the radius of the deposit is measured at $r=R_d$ and $z=h=0$, we finally find

$$\frac{d\rho_d}{dT} = \cos(\vartheta)\frac{K^* P}{2D_C}\int_0^\infty J_0(Q\rho_d)F(T,Q)\exp(-Q^2/4)QdQ, \qquad (4)$$

where $J_0(x)$ is the zeroth-order Bessel function and ϑ is the contact angle of the deposit on the substrate. In this equation, we have also rescaled all the length and time variables by using, respectively, the beam radius a_0 and the mass diffusion time scale over a_0. Definitions are thus: $\rho_d=R_d/a_0$, $W=\sigma a_0$, and $T=D_C t/a_0^2$. Finally, Q represents the conjugate Fourier-Bessel mode associated to the rescaled radial variable $R=r/a_0$. $F(T,Q)$, given by,

$$F(T,Q) = \frac{1}{Q^2-W^2}\{-W + Q\ \mathrm{erf}(Q\sqrt{T}) + W\exp[-(Q^2-W^2)T]\mathrm{erfc}(W\sqrt{T})\}, \qquad (5)$$

describes the temporal behavior of the diffusive flux normal to the deposit. Note that contrary to the diffusive mechanisms that govern the kinetics of laser-induced liquid/liquid phase transitions in nonabsorbing liquid mixtures [20], where the droplet feeding is ensured by the radial mass flux, the deposit growth is here totally controlled by the diffusive flux along the beam axis $D_C(\partial\Phi_C/\partial Z)_H$ because the solute adsorption condition implies $(\partial\Phi_C/\partial R)_H=0$ at the deposit boundary. While Eq. (4) gives the general expression for the growth rate after the nucleation stage, experiments are generally conducted in adiabatic conditions [21]. This means that growth is analyzed over a period much larger than the mass diffusion time scale to consider that the solute concentration around the growing deposit is almost stationary. Then, $F(T,Q)$ reduces to $F(T,Q)|_{adiab}=1/(Q+W)$, and we find

$$\left.\frac{d\rho_d}{dT}\right|_{adiab} = \cos(\vartheta)\frac{K^* P}{2D_C}\int_0^\infty \frac{J_0(Q\rho_d)\exp(-Q^2/4)}{Q+W}QdQ. \qquad (6)$$

Practically, photodeposition requires in any case a "reasonably" important optical absorption σ. Then, we see from Eq. (6) that the rescaled absorption W plays a major role in the growth rate. However, at a given absorption σ, W can be made large or small compared to one depending on the beam size. Then, different growth regimes are expected to occur according to the amplitude of the rescaled optical absorption. Analysis of these regimes is the purpose of the following sections.

A second important and complementary aspect is the description of the deposit height $h_d = h(r=0)$. Two different approaches disserve investigation to probe experimentally the temporal behavior of h_d. At first, considering our spherical model, the height h_d of the deposit on beam axis is related to its radius R_d and to the contact angle ϑ by the relation $h_d = [(1-\cos\vartheta)/\sin\vartheta]R_d$. Since this expression is deduced from a droplet growth model, it means that wetting and surface tension dominate the deposit shape. While these assumptions can be reasonable for vanishing deposit heights, this reasoning becomes disputable for larger deposit thickness because the exciting beam is usually attenuated within the deposit. Consequently, we need to take into account the optical absorption of the deposit and remove any surface tension forcing. Doing this, and assuming that the shape of the deposit at nonvanishing height is represented by a beam centered surface of revolution, the temporal behavior of the deposit thickness on beam axis becomes

$$H_d = \frac{1}{W'}\ln\left[1 + \frac{K^* W' P}{2D_C}\left(\int_0^\infty \frac{\exp(-Q^2/4)}{Q+W} Q dQ\right) T\right], \quad (7)$$

where $H_d = h_d/a_0$ is the reduced deposit height, and $W' = \sigma' a_0$ is the rescaled optical absorption of the deposit. Equation (7), which shows a behavior at variance from that predicted for the deposit radius, is also known as the Elovich growth equation [10]; it was empirically used to describe the growth of thin amorphous selenium film photodeposited from colloidal solutions under laser excitation [22].

B. Radial growth at large rescaled optical absorption

The experimental setup and an example of late stage radial growth of a photodeposit are presented in Fig. 1. The sample is horizontally mounted in the (x,y) plane and illuminated with a white light source. The exciting beam is injected vertically (z direction) within the sample by a first beam splitter and rejected by a second one to protect the charge coupled device (CCD) video camera from laser radiation. The induced deposit is observed with the CCD video camera using an ocular of focal length 35 mm. The photodeposit evolution is also digitized in logarithmic time scale, by means of a frame grabber for the acquisition. A third lens (not shown) is located before the first beam splitter to focus the beam at the entrance face of the cell; lenses with different focal distances are used to vary the beam waist [23].

Nucleation of a Cr(III) precipitate occurs as soon as the solubility limit is reached, and a photodeposit starts to coat the substrate (entrance glass slide) intercepted by the laser beam; silanization of the cover slip prevents any deposition on the exit window of the cell. While we will not analyze nucleation processes of a photodeposit, the second stage of the growth, i.e., the fractal aggregation between growing spheroids and their internal restructuring inside the whole structure is illustrated in Fig. 2; we present binary images to enhance the involved mechanisms. When looking at the time associated to pictures, we see that the fractal structure rapidly disappears to give birth to a compact layer.

Due to the observed internal reorganization and the resulting increase in compactness, the image processing used to analyze the late-stage growth regime of the photodeposit consists in approximating the surface coverage measurement by the area of a circular domain of mean radius $R_d(t)$. Note that such a procedure cannot be implemented at earlier time. Using this procedure, Fig. 3 shows measurements over a wide region of the optical parameter space: $7 \leqslant P \leqslant 42$ mW and $81 \leqslant a_0 \leqslant 345$ μm (i.e., over almost two orders of magnitude in incident beam intensity). Growth is clearly an increasing function of the exciting beam intensity. While no particular scaling seems to emerge from these measurements, two growth regimes are nevertheless evidenced. A large growth rate regime at early time is followed by a short crossover to a slow late-stage growth. Considering the pictures given in Fig. 2 in relation to their associate time, we can confidently relate the first regime to the early stage growth, where the reorganization of the growing fractal deposit dominates.

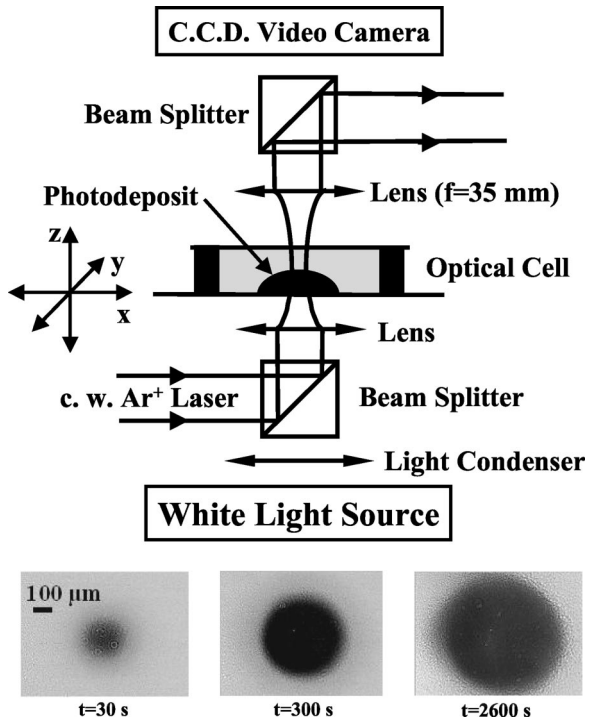

FIG. 1. Schematic representation of the experimental setup implemented to analyze the radial growth of circular photodeposits. An example is presented below for an incident beam power $P = 12.8$ mW and a beam waist $a_0 = 143$ μm.

To interpret these data, we apply our "droplet growth" model to the large rescaled optical absorption case. Due to the $\exp(-Q^2/4)$ term appearing in the expression of the deposit growth rate given by Eq. (6), the integral contribution for $Q > 2$ is almost negligible. Consequently, if we rescale time by taking $\tau = \cos(\vartheta)(K^* P/D_C W)T$, instead of T, the late stage growth rate for $W \gg 1$ reduces to a very simple universal form:

$$\left.\frac{d\rho_d}{d\tau}\right|_{W\gg 1} = \exp(-\rho_d^2). \quad (8)$$

Interest in this new form of the growth rate is that the entire dependence in exciting beam parameters is transferred to

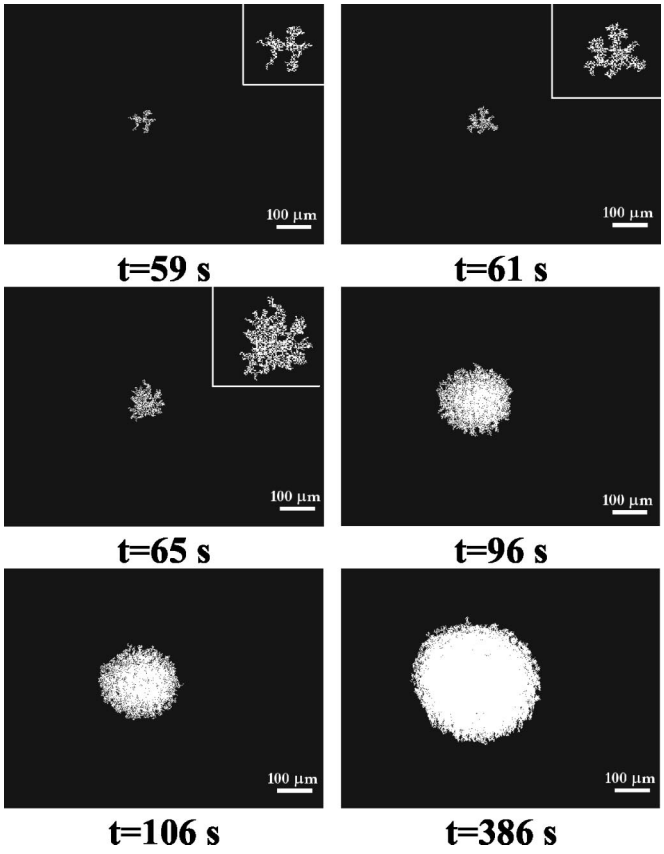

FIG. 2. Temporal behavior of the deposit compactness by fractal aggregation between growing spheroids and internal restructuring. Insets are enlargements to observe the evolution of the fractal structure. The incident beam power and the beam waist values are respectively $P=3$ mW and $a_0=155$ μm.

both the rescaled deposit radius and the new time scale which now behaves as $\tau \propto Pt/a_0^3$.

According to this model, the data set should therefore point out a single-scaled dynamics of the late-stage growth if the radius of the deposit is rescaled with a_0 and the time with a_0^3/P. This data reduction is shown in Fig. 4 for the whole set of experiments presented in Fig. 3. The scaling is robust from the early to the late stage of the growth. It also enhances and demonstrates the existence of the well-defined crossover between the two regimes. From a quantitative point of view, the expected late-stage behavior is recovered experimentally. We use the growth rate $(a_0^3/P)d\rho_d/dt = \alpha \exp[-(\beta\rho_d)^2]$, with the initial condition for integration $\rho_d(t=0)=0$, to fit the whole data set. We find $\alpha = 10\pm 2$ $\mu m^3/\mu J$ and $\beta = 1.1\pm 0.1$ by taking into account errors on P and a_0 that are $\Delta P/P = \Delta a_0/a_0 \approx 5\%$. The value of β is very close to one, in agreement with the Gaussian dependence of the growth rate predicted by Eq. (8). On the other hand, for $\rho_d \lesssim 0.5$ our droplet model is obviously not appropriate to fit the transient acceleration of the kinetics driven by the fractal aggregation stage. Moreover, the use of our experimental procedure for fractal deposits leads necessarily to an overestimation of the amplitude α compared to that predicted for pure solute adsorption on a single seed. Nevertheless, the fact that a data reduction is also observed

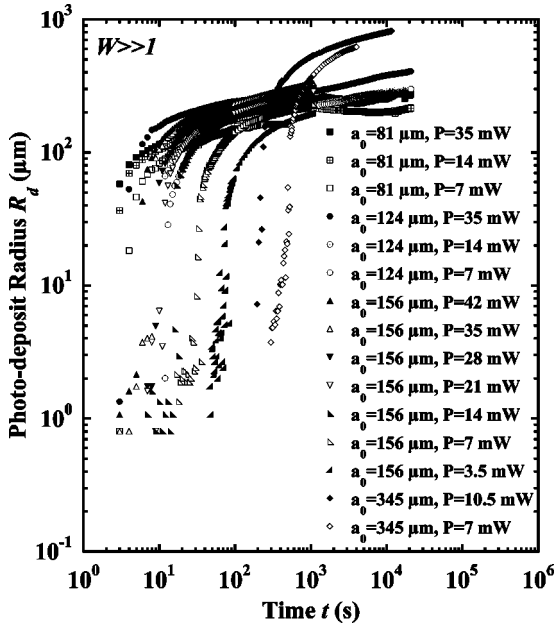

FIG. 3. Photodeposit growth for large values of the rescaled optical absorption. The region of the optical parameter space scanned ($7 \leqslant P \leqslant 42$ mW and $81 \leqslant a_0 \leqslant 345$ μm) leads to an incident beam intensity variation within the range 1.9 W/cm^2 to 170 W/cm^2.

for the fractal structure during the aggregation and reorganization stage strongly suggests that particle adsorption is the main driving mechanism for photodeposit growth. Then, unlike laser-induced liquid-liquid phase separation [20], the Gibbs-Thomson effect [21] is no more required to drive the

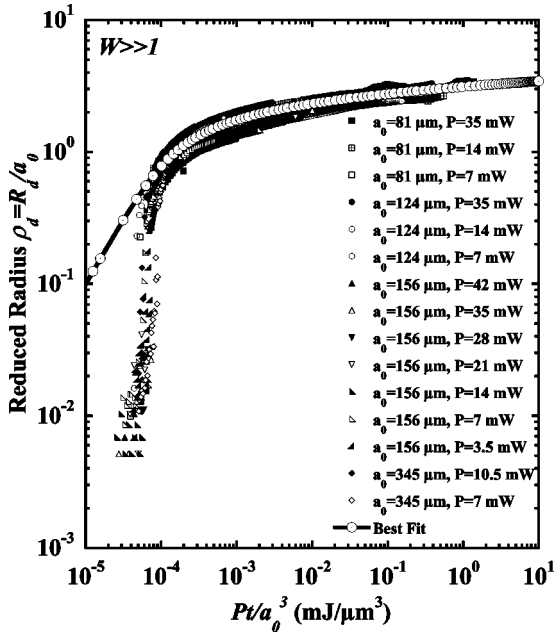

FIG. 4. Plot in reduced variables $(\rho_d = R_d/a_0, Pt/a_0^3)$ of the fifteen experiments presented in Fig. 3. The separation between the aggregation regime and the late-stage growth is clearly enhanced by the scaling. The solid line represents the best fit of the late-stage deposit growth performed according to Eq. (8).

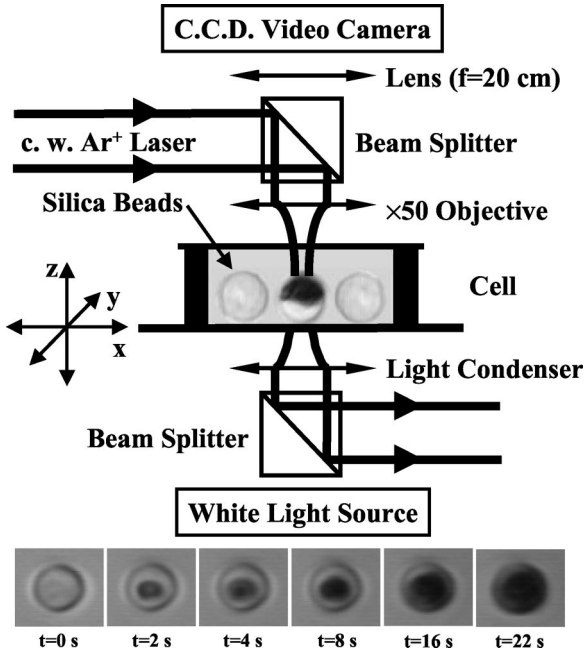

FIG. 5. Schematic representation of the experimental setup implemented to analyze the radial growth of a circular coating photodeposited on one hemisphere of a microparticle, as that illustrated by the side view of a 10-μm-silica bead centered on the beam. An example is presented below. The incident beam power and the beam waist values are respectively $P=35$ μW and $a_0=0.42$ μm.

growth of a photodeposit after the nucleation of spheroids.

For practical applications, this unified description is of particular interest because the agreement between theory and experiments shows that one can confidently control the dynamic organization of photodeposition, and even predict its evolution. Moreover, bearing in mind that our model contains basic ingredients of photochemical deposition, it should be extended to any photodeposit driven by a one-photon absorption, such as photochemical deposition of noble metals [24] or semiconductors [25].

C. Radial growth at small rescaled optical absorption

To illustrate an application of laser-driven photodeposition, we investigate the growth regime associated to a small rescaled optical absorption by analyzing the kinetic control of the partial coating of microparticles, instead of describing the more classical situation of deposition onto a flat substrate; the flat substrate case is simply illustrated at the end of the section. This approach also shows how deposition methods can be extended to curved surfaces. The experimental setup is presented in Fig. 5. As in the preceding experiment, the photochemical reaction is driven by a linearly polarized TEM_{00} Ar^+ laser. Microparticles are now added and dispersed in the liquid mixture. We used 10-μm NUCLEOSIL® silica beads for liquid phase chromatography purchased from Macherey-Nagel. Samples are enclosed in a very thin tight homemade cell, composed of a glass slide and a cover slip separated by 30-μm thickness mylar spacers, to prevent disturbing thermal effects induced by the light absorption. The cover slip was as well silanized to eliminate any photochemical deposition on the entrance face of the cell. The cell is horizontally mounted to keep the beads at rest on the bottom plate. A computer controls translation stages, with step accuracy of 0.5 μm, to move the holder in the three directions. To observe the growth of a deposit on top of a bead, the experimental setup is reverted compared to that presented in the preceding section. The incident beam power P is adjusted with a rotating half-wave plate (not shown) located before the first beam splitter. Laser-assisted microphotochemical deposition is monitored by a long working distance $\times 50$ microscope lens (numerical aperture NA=0.5) that focuses the beam on the top hemisphere of a bead; at the focus, the beam radius is $a_0=0.42$ μm. Note that, despite the curvature of the substrate, the relative position of the focus versus the microsphere surface intercepted by the beam is not very critical because the cylindrical wave symmetry along the propagation axis can be assumed for axial distances $|z| \leqslant z_d = \pi n \omega_0^2/\lambda_0 \approx 3$ μm from the focus. Imaging of the coating photodeposited on a bead is made by the conjugation of the $\times 50$ microscope objective with a second lens ($f=20$ cm) on the CCD video camera which is coupled to a computer for the frame acquisition.

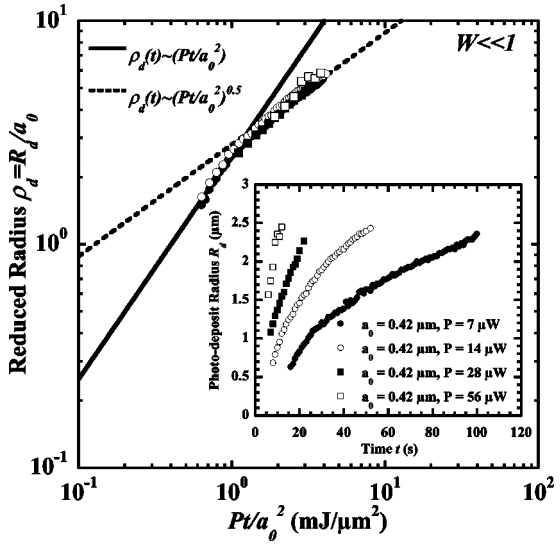

FIG. 6. Plot in reduced variables $(\rho_d=R_d/a_0, Pt/a_0^2)$ of the growth of the coating deposited on top of a beam centered 10-μm-silica beads presented in the inset for increasing beam power excitations. The solid line represents a fit of the linear regime $\rho_d(t) \propto Pt/a_0^2$ expected at the very beginning of the growth when the deposit does not feel yet the Gaussian nature of the exciting wave. The dashed line corresponds to the power law fit $\rho_d(t) \propto \sqrt{Pt/a_0^2}$ expected for $\rho_d(t) \gg 1$.

An example of photodeposit growth on top of the bead hemisphere intercepted by the beam is also presented in Fig. 5. Since the substrate is curved and growth mechanisms involve solute flux along the axial direction, the image processing approximates the measured cross section of the covered hemisphere by a circular area of radius $R_d(t)$instead of considering the surface really covered by the deposit [26]. The inset of Fig. 6 shows measurements carried out at $a_0=0.42$ μm over almost one order of magnitude in incident

beam power $7 \leqslant P \leqslant 56$ μW. While they show that growth rate is an increasing function of the optical excitation, the transient acceleration expected at the early stage growth is not evidenced, contrary to the large optical absorption case.

To interpret these data, we continue to apply our "droplet growth" model, but now to the small optical absorption case. Then, W is neglected in Eq. (6). In this case, if we rescale time by taking $\tau' = \cos(\vartheta)(\sqrt{\pi K^* P/2 D_C})T$, instead of T, the radial growth rate reduces to a very simple universal form:

$$\left.\frac{d\rho_d}{d\tau'}\right|_{W \ll 1} = \exp(-\rho_d^2/2) I_0(\rho_d/2), \tag{9}$$

where I_0 is the zeroth-order modified Bessel function. The new time scale now behaves as $\tau' \propto Pt/a_0^2$. According to Eq. (9), the data set should point out a second single-scaled dynamics of the late-stage growth if time is rescaled with a_0^2/P while the radius of the deposit is still normalized by a_0. This data reduction on a master curve is shown in Fig. 6. Note that a very simple asymptotic regime emerges in this low optical absorption case. Indeed, using the relation $I_0(x) \approx \exp(x)/\sqrt{2\pi x}$ for $\rho_d \gg 1$, we find $\rho_d|_{W \ll 1} \propto \sqrt{\tau'}$ at large rescaled deposit radius in good agreement with observations (a power law fit leads to $\rho_d|_{\substack{W \ll 1 \\ \rho_d \gg 1}} = 2.65(Pt/a_0^2)^{0.56}$ when Pt/a_0^2 is expressed in mJ/μm^2). This leads to $R_d \propto \sqrt{\sigma(Pt)}$, which shows that growth does not feel the influence of the beam waist a_0 when the deposit radius becomes much larger than that of the excitation size, and simply depends on the energy deposited in the medium. Agreement is also observed at smaller ρ_d for which the regime $\rho_d|_{W \ll 1} \propto \tau'$ is predicted. Indeed, if Pt/a_0^2 is expressed in mJ/μm^2, then a power law fit of the concerned data leads to $\rho_d|_{\substack{W \gg 1 \\ \rho_d \gg 1}} = 2.88(Pt/a_0^2)^{1.1}$. On the other hand, to get some insight on the growth amplitude we perform a fit of the whole data set according to the following growth rate:

$(a_0^2/P)d\rho_d/dt = \alpha \exp[-(\beta\rho_d)^2] I_0[-(\beta\rho_d)^2]$, with the initial condition for integration $\rho_d(t=0)=0$. However, we find $\alpha = 3.2$ μm^2/ μJ and $\beta = 0.07$ which are at variance with expectations. Since we recovered the right growth exponents, this discrepancy could as well be explained by the existence of a transient growth acceleration at the very early stage. As we now evidence the $\rho_d|_{W \ll 1} \propto \tau'$ regime, this means that transient acceleration occurs at a time much smaller that that observed for $W \gg 1$, but still exists.

From the practical point of view, this low rescaled absorption regime is more appealing to pattern surfaces because it leads to the realization of the finest structures. See, for example, the different periodic patterns realized on one hemisphere of a microparticle [Figs. 7(a) and 7(b)] or the kinetic control of a dot grating deposited on a flat substrate [Figs. 7(c) and 7(d)]. As in the previous case, the agreement observed between theory and experiments strongly suggests that these photodeposited patterns can easily be controlled externally. Consequently, using a serial procedure, Figs. 7(c) and 7(d) show that one can totally tailor the spatial arrangement of a holographic grating as well as its optical phase and amplitude properties by controlling growth of the different deposited patches. Applications of the asymmetric patterning

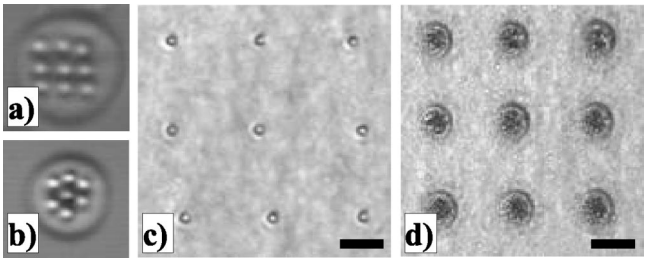

FIG. 7. Periodic photodeposition at $W \ll 1$ performed by a computed matrix addressing of the x and y translation stages. (a) and (b) Micro arrays deposited on 10 μm-silica beads. The incident beam power, the beam waist, and the exposition time values are, respectively, $P = 28$ μW, $a_0 = 0.42$ μm, and $t_e = 5$ s. The dot size is approximately 1 μm. (c) and (d) Dot grating deposited on glass substrate at two successive exposition times. The incident beam power and the beam waist are $P = 0.3$ mW and $a_0 = 0.9$ μm while the exposition time values are respectively $t_e = 2$ s (c) and $t_e = 10$ s (d). Bare scales are 10 μm.

of microspheres can as well be devised in numerous emerging areas. A direct extension of the previous point is the tailoring of the phase and the amplitude of microlens coating in optoelectronics devices [27]. Another important feature is the chemical anisotropy resulting from dissymmetrization of microparticle hemispheres. Indeed, the induced coating can be further functionalized or used as a mask to chemically modify the uncoated surface. In a second step, the deposit can be removed allowing a further different functionalization of the previously covered surface [28]. Unsymmetrical microspheres can finally be used as "rectified" elements which can self-assemble in a privileged fashion to build organized architectures, such as photonic crystals [29].

D. Radial growth at intermediate rescaled optical absorption and discussion

The experimental setup used to analyze this regime was either that presented for the $W \gg 1$ study or that implemented to coat microparticles, where the microscope objective is changed to obtain intermediate beam waists. Figure 8 shows rescaled measurements for $0.9 \leqslant P \leqslant 7$ mW and $5 \leqslant a_0 \leqslant 11$ μm. To interpret these data, we cannot apply any asymptotic regime in W (experiments correspond to $0.07 \leqslant W \leqslant 0.14$) and we must use the general form of the deposit growth rate given by Eq. (6). In this case, no particular rescaled time, neither $\tau \propto Pt/a_0^3$ nor $\tau' \propto Pt/a_0^2$, emerges to reduce the data set to a master curve; we are typically in a crossover regime.

To get a global view and discuss some general properties of radial growth driven by laser photochemical deposition, we also plot in Fig. 8 a representative sampling of the full experimental set in reduced variables $(\rho_d = R_d/a_0, Pt/a_0^3)$ obtained for all the regimes in rescaled optical absorption. The main interest in such a presentation is that temporal behaviors of growth laws in different regimes are not sufficient to understand growth. Amplitudes of growth rates and the comparison between these amplitudes are also of great importance to characterize growth mechanisms. It clearly appears

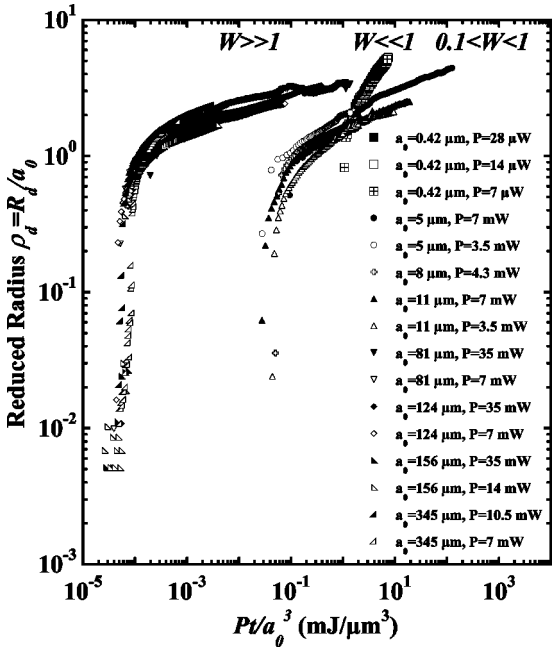

FIG. 8. Plot in reduced variables ($\rho_d = R_d/a_0, Pt/a_0^3$) of the photodeposit growth laws measured for the $W \ll 1$, the intermediate W (eight experiments), and the $W \gg 1$ regimes.

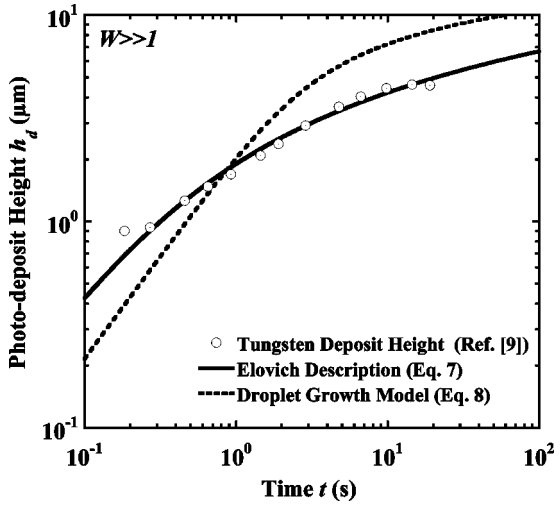

FIG. 9. Temporal behavior of the height of a tungsten spot photodeposited by excitation of a WCl_6 vapor with a dye laser operating at $\lambda_0 = 680$ nm. The incident beam power and the beam waist values are respectively $P = 270$ μW and $a_0 = 5$ μm. The solid and the dashed lines correspond to fits, respectively, performed according to Eq. (7) (Elovich equation) and Eq. (8) (droplet growth model at large rescaled optical absorption).

in Fig. 8 that the two asymptotic situations $W \ll 1$ and $W \gg 1$ are well separated in reduced time and that the intermediate W regime is in between the two others. An increase in W leads to a shift towards smaller Pt/a_0^3. This behavior is in qualitative agreement with predictions. However, from a quantitative point of view, when data are plotted versus Pt/a_0^2 as illustrated in Fig. 6 of Part I, instead of Pt/a_0^3, this situation should revert. Indeed, when time is rescaled according to the mass diffusion time scale, growth in the $W \ll 1$ ($W \gg 1$) regime becomes the fastest (slowest). However, while the intermediate W case and the $W \ll 1$ regime revert together as expected, our experimental data show that the $W \gg 1$ case still corresponds to the fastest regime, which is in contradiction with our model. This discrepancy regarding the full data set could be understood from the growth mechanisms observed at early time (see Fig. 2). Indeed, the transient fractal aggregation between growing spheroids and the internal restructuring inside the whole structure observed at large W considerably accelerate the kinetics of deposition at its early stage. While we have seen that there is no obvious reason to remove this process in the $W \ll 1$ case, its influence is nevertheless strongly attenuated because $W \ll 1$ experiments are realized by decreasing the beam waist instead of reducing the optical absorption of the initial photosensitive solution. Consequently, at the very early stage of the growth, the number of spheroids nucleated in the illuminated area is much smaller than that obtained for $W \gg 1$, which leads to a strong decrease of the transient acceleration due to the rearrangement of the initial fractal deposit. So, even if we are mainly interested here in the late stage growth of a photodeposit, this analysis clearly shows how it can be influenced by the preceding stages.

E. Late stage growth of the deposit thickness

As our experimental setup does not allow reliable *in situ* measurements of the kinetic behavior of the height of single deposits, the confrontation between theory and experiments presented in this section is based on data already published in the literature. Even if we found several analyses devoted to kinetic behaviors of photodeposition in various systems (cadmium [30], gold [31], selenium [19], or tungsten [32] spot deposition for instance), very few can be used to check our model for the following reasons. At first, most of them investigate the early growth stage where the deposit height varies almost linearly in time [30,31]. To investigate this issue, we proposed two different approaches, one based on the radial growth using $h_d = [(1-\cos\vartheta)/\sin\vartheta]R_d$ and the other leading to the Elovich equation given by Eq. (7). However, both descriptions lead to a linear temporal variation of the height at the early stage growth, and thus prevent us to make a clear-cut choice. On the other hand, our model consider a Gaussian excitation at a given optical wavelength. Therefore, experiments performed under optical excitation by spectral lamps [19,31] cannot be interpreted as far as the intensity distribution of the light source is not known. Consequently, to illustrate deposit height growth, we consider the case of laser-induced tungsten deposition analyzed in Ref. [32] and presented in Fig. 16.2.3a of Ref. [9], where measurements are presented over three orders in magnitude in time. Data are shown in Fig. 9. Excitation is performed with a dye laser operating at $\lambda_0 = 680$ nm. The incident beam power and waist are, respectively, $P = 270$ mW and $a_0 = 5$ μm. To compare these measurements to our model, we perform two fits. The first one is realized according to Eq. (8), which gives the radial growth rate predicted for large rescaled optical absorption (the precursor WCl_6 is supposed to strongly absorb light) and by replacing R_d by R_d

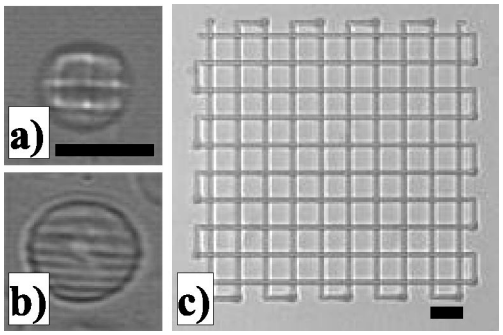

FIG. 10. Periodic photodeposition at $W \ll 1$ performed by computed continuous scanning of the x and y translation stages. (a) and (b) Microarray deposited on 10-μm-silica beads. The incident beam power, the beam waist, and the scanning rate values are respectively $P=42$ μW and $a_0=0.42$ μm, and $V_S=1$ μm/s. Features slightly smaller than 1 μm are observed. (c) Line array deposited on a glass slide. The incident beam power, the beam waist, and the scanning rate values are respectively $P=0.3$ mW, $a_0=0.9$ μm, and $V_S=5$ μm/s. Bare scales are 10 μm.

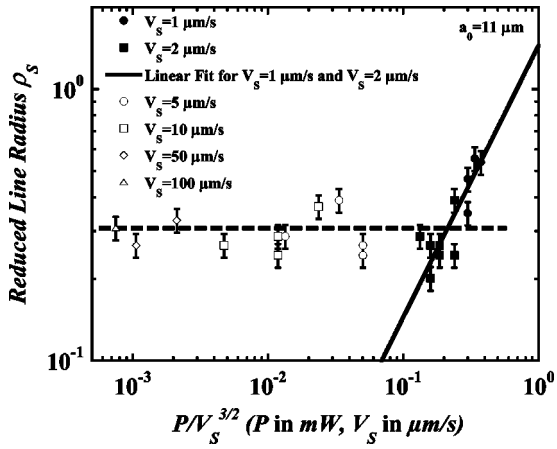

FIG. 11. Rescaled width of photodeposited lines versus incident power P and scanning velocity V_S at $W=0.15$. The solid line represents a linear fit of the expected behavior for $V_S=1$ μm/s and $V_S=2$ μm/s. The dashed line is a guide for the eye to point out a saturation of the linewidth observed at larger V_S.

$=[\sin\vartheta/(1-\cos\vartheta)]h_d$. As illustrated in Fig. 9, this hypothesis cannot fit data at all. The second approach considers the Elovich form given by Eq. (7). By using $h(t)=\alpha\ln(1+\beta t)$, we find $\alpha=1/\sigma'=1$ μm and $\beta=4.8$ s^{-1} with 10% errors. Note that the α value leads to a deposit absorption $\sigma'=10^6$ m^{-1} that is in qualitative agreement with that of pure tungsten ($\sigma_W=30\times10^6$ m^{-1}). Consequently, it seems that the temporal behavior of the height of high optical absorption deposits is governed by an Elovich equation as already postulated in selenium film deposition analyses [22]; the droplet growth model, which supposes that surface tension governs the shape of the deposit, fails to predict the height behavior at late stage. Further investigations are nevertheless required due to the fact that we did not fit a large set of data.

IV. GROWTH OF PHOTODEPOSITED LINES

A practical extension of the developments presented in the preceding sections consists in describing the effect of a scanning beam in order to write continuous patterns on the substrate instead of dot assemblies. Indeed, the use of laser beams to build interconnects [3], to repair microelectronic circuit defects [4], or to create continuous patterns of surfaces with microscopic features [33,34], constitutes an appealing alternative to conventional lithography. Examples of such surface patterning on 10-μm-silica beads and glass substrate are presented in Fig. 10 for the $W \ll 1$ regime.

The most interesting situation for application purpose concerns the deposition of narrow lines [35], as those shown in Fig. 10. However, to give an overview of the properties of line writing by photochemical deposition, we present in the following experiments realized at larger W but still in the $W \ll 1$ regime. By denoting with V_S the beam scanning velocity, the normalized characteristic time of deposition is given by $T_S=D_C t_S/a_0^2$, where $t_S=2a_0/V_S$ corresponds to the time required to scan a beam diameter. For scanning velocities of the order of a few microns per second, one has $T_S \ll 1$. Photodeposition during T_S is thus described by the early stage growth regime where the adiabatic approximation does not apply yet. One should therefore take into consideration the time dependence of $F(T,Q)$ in the general growth rate equation [Eq. (4)]. The expression of $F(T,Q)$, given by Eq. (5), reduces to $F(T,Q) \underset{T\ll1}{\approx} (2/\sqrt{\pi})\sqrt{T}$ for $T \ll 1$. So, as far as line writing is performed during a scanning time $T_S \ll 1$, the condition $\rho_d \ll 1$ is verified and the line radius is given by

$$\rho_S \underset{T_S\ll1}{\approx} \cos(\vartheta)K^*\frac{8\sqrt{2}}{3\sqrt{\pi}}\sqrt{D_C}\frac{P}{(a_0V_S)^{3/2}}, \tag{10}$$

where $\rho_S=\rho_d(T=T_S)$. Equation (10) shows that, if the beam waist a_0 is held constant as in most experiments, the wideness of the written line can be dynamically monitored in a very smart way by the ratio $P/V_S^{3/2}$ where two external parameters, i.e., P and V_S, can be adjusted independently according to the experimental conditions. In highly absorbing media it is preferable to choose low laser power excitations to prevent any alteration induced by thermal decomposition and adjust the amplitude of the scanning velocity, while in the opposite case larger variations in P are confidently achievable. In fact, experiments are much more sensitive to the choice of the couple (P,V_S) than expected. At low powers and/or high scanning velocities, lines are discontinuous and bubbly due to the influence of nucleation. In the opposite case (large powers and/or small velocities) disturbing thermal effects become rapidly dominant, leading to a blurring of the line writing process. Thus, the investigable window in (P,V_S) to observe well-written lines as those presented in Fig. 10(c) is narrow. Figure 11 presents experiments realized in these conditions at $a_0=11$ μm for $1 \leqslant V_S \leqslant 100$ μm and $0.15 \leqslant P \leqslant 0.75$ mW.

While experiments are in reasonable agreement with predictions at low scanning velocities [for which the linear variation predicted by Eq. (10) is recovered], a saturation in rescaled line width occurs at larger V_S (typically for V_S

$\geqslant 5$ μm/s), i.e., for smaller exposition time $t_S = 2a_0/V_S$. This disagreement could originate in part from the processing of images captured from optical microscopy because diffraction effects increase drastically for decreasing line widths and prevent any reliable measurement of widths smaller than 2 μm. However, a physical origin can also be stressed because for our particular system, we have seen above that growth at the early stage is fractal, which leads to an over estimation of the mean deposit size. To avoid this effect and retrieve the expected scaling, deposited lines must therefore be compact. But at short time, such a restrictive situation requires a strong increase in beam power excitation, which unfortunately leads to liquid boiling and destruction of the deposit.

V. GROWTH OF SURFACE RELIEF GRATINGS

A. Theoretical background

To build surface relief gratings by photochemical deposition, we consider two linearly polarized TEM_{00} Gaussian beams of same intensity that interfere on the substrate with an angle ψ. The light intensity distribution that excites the photosensitive liquid mixture is written as

$$I(X,Z) = \frac{P}{\pi a_0^2}[1 + \cos(Q_0 X)]\exp(-WZ), \qquad (11)$$

where $Q_0 = 2\pi a_0/\Lambda_0$ is the rescaled Fourier wave vector associated to the fringe spacing $\Lambda_0 = \lambda_0/[2n \sin(\psi/2)]$ forced by the two interfering beams. P corresponds to the total power injected in the medium. In experiments, we fulfill the condition $Q_0 \gg 1$ to justify the plane wave approximation used to write Eq. (11). Then, the temporal behavior of the relief of the induced deposit is obtained by extending the calculation of the growth rate of the deposit thickness driven by one beam [Eq. (7)] to a two-wave excitation (Sec. V in Part I). We showed that the dynamics of the scaled height of the modulated deposit $H_d(T)$ is described by a logarithm variation of the sum of two contributions: a background represented by the $Q=0$ mode, which corresponds in fact to the contribution of the Gaussian envelop of the pump waves, and a modulation driven by the forced mode $Q=Q_0$. However, when working with holographic gratings it is useful to separate as much as possible the background contribution to that of the modulation because the former often acts as an amplitude pedestal (its optical phase shift is constant) while the latter gives the phase shift required to characterize the diffraction properties. To do so, we use the properties of the function $F(T,Q)$. As $F(T,Q) \underset{T \ll 1}{\approx} (2/\sqrt{\pi})\sqrt{T} \ll 1$ at the early stage growth and $F(T,Q=Q_0) \ll F(T,Q=0)$ at later time, the influence of the logarithmic variation of H_d is in fact weak. H_d can then be decomposed as $H_d(X,T) \approx \overline{H_d}(T) + [\Delta H_d(T)/2]\cos(Q_0 X)$, where the background and the modulation contributions are, respectively, given by

$$\overline{H_d}(T) = \frac{1}{W'}\ln\left[1 + \frac{K^* W' P}{D_C}\int_0^T F(T',Q=0)dT'\right],$$

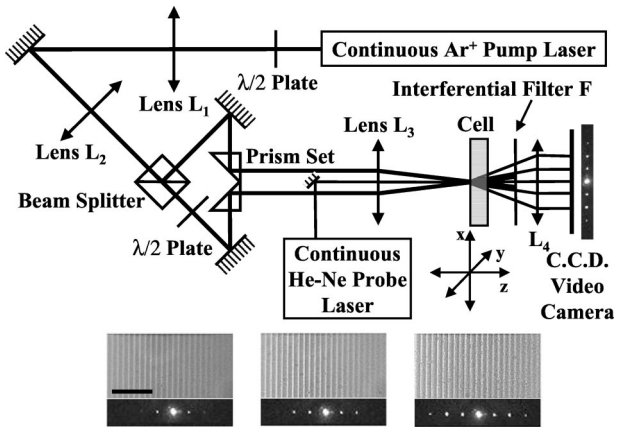

FIG. 12. Experimental setup used to induce a photodeposited surface relief grating and probe its optical characteristics. The angle ψ between the two pump beams is adjusted by moving the two-prism system along the z direction. The beam waist at the entrance of the cell ($a_0 = 156$ μm) is monitored by imaging the beam waist generated at the focus of the lens L_1 with the afocal system L_2-L_3. The beam waist of the probe beam is $a_0 = 90$ μm. The lens L_4 is used to image the dynamics of the diffraction pattern of the probe on the CCD video camera. An example of surface relief grating evolution at the emergence onset of the first, the second, and the third order of diffraction is presented below. The incident beam power and the fringe spacing between the pump beams are respectively $P = 35$ mW and $\Lambda_0 = 6$ μm. The bare scale is 50 μm.

$$\Delta H_d(T) = \frac{2K^* P}{D_C}\frac{\displaystyle\int_0^T F(T',Q=Q_0)dT'}{\displaystyle 1 + \frac{K^* W' P}{D_C}\int_0^T F(T',Q=0)dT'}. \qquad (12)$$

As experimentally illustrated below, this separation is of particular importance when deposits become thick and the number of diffraction orders increases because classical models [36] are generally based on thin sine profiles and first-order diffraction response.

B. Results and discussion

The experimental setup is illustrated in Fig. 12. The modulated deposit is now created by splitting the beam into two parts of equal intensity and path length. These two pump beams are then recombined and intersect at the entrance window of the sample with an angle ψ, building up a spatially periodic intensity distribution characterized by the spatial wave vector $q_0 = 2\pi/\Lambda_0$. The center of the induced grating is optically probed by a continuous He-Ne laser (wavelength in vacuum $\lambda_p = 633$ nm) of sufficiently low power to avoid any coupling with the deposition process. The beam waist $a_0 = 90$ μm of the probe is smaller than that of the pumps inside the sample ($a_0 = 156$ μm). An example of photodeposited grating dynamics, as well as the associated diffraction pattern [37], is also presented in Fig. 12. The temporal evolution of the diffraction pattern is digitized by means of a charge coupled device video camera coupled to a frame grabber.

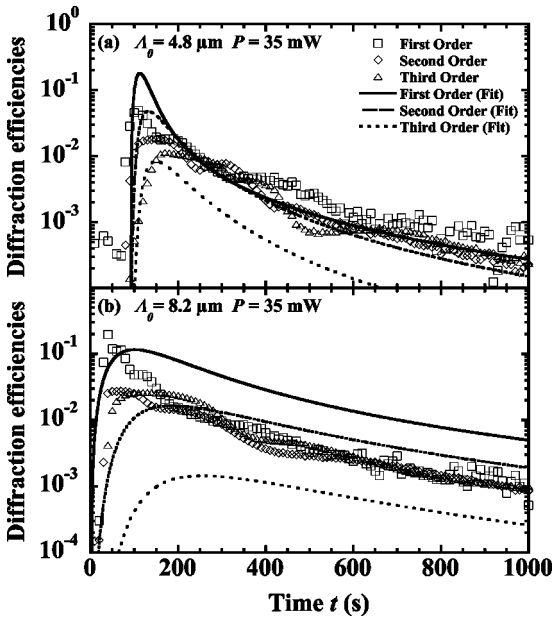

FIG. 13. Measured efficiency of surface relief gratings deposited by two pump beams interfering for a total incident beam power $P=35$ mW and two values of the fringe spacing: (a) $\Lambda_0=4.8$ μm and (b) $\Lambda_0=8.2$ μm. Fits are performed according to Eq. (13).

As suggested by Fig. 12, dynamic characterizations of grating relief can be realized by analyzing the evolution of the resulting laser probe diffraction pattern. In Fraunhoffer conditions, the probe amplitude diffracted by the photodeposit in the u direction is given by the Fourier transform of the modulation transfer function $f_{trans}(x,t)=\eta(x,t)e^{i\varphi(x,t)}$, where $\eta(x,t)=\exp[-\sigma' h_d(x,t)]$ and $\varphi(x,t)=2\pi\Delta n h_d(x,t)/\lambda_p$ are, respectively, the absorption and the phase shift contributions (Δn is the refractive index difference between solution and deposit). The phase shift induced by the pedestal $\overline{h_d}(t)$ is constant in space; it can be discarded. On the other hand, according to Eq. (12), the beam attenuation associated with the modulation Δh_d is negligibly small compared to that of the pedestal. So, as the amplitude of the wave $E_{m=0,\pm1,\pm2,\ldots}$ diffracted by the relief grating is given by the mth Fourier component of the modulation transfer function $E_m(t)=(E_p/\Lambda_0)/\int_0^{\Lambda_0} f_{trans}(x,t)e^{im2\pi x/\Lambda_0}dx$ [38], where E_p is the incident field amplitude of the probe, one finally finds that the diffraction efficiency ε_m of the mth order is given by

$$\varepsilon_m=|E_m|^2/|E_p|^2\approx e^{-2\sigma'\overline{h_d}}\left|J_m\left(\frac{2\pi\Delta n}{\lambda_P}\frac{\Delta h_d}{2}\right)\right|^2, \quad (13)$$

where $J_m(x)$ is the mth order Bessel function. Two examples of mean temporal evolution of the first three diffraction order efficiencies are illustrated in Fig. 13 for two values of the fringe spacing Λ_0.

Note that, contrary to the growth of photodeposited circular patches (Sec. III), we observe an ignition time $t_{ignition}$ associated with the delay required to reach the solubility of $Cr(OH)_3$ before deposition occurs. This is not surprising since optical diffraction analyses are always more sensitive than direct observations. Using Eq. (13) to fit the set of experiments presented in Fig. 13, we find $\Delta n=1$, $\sigma'=6\times10^4$ m^{-1}, and $K^*=8\times10^{-9}$ m^2/J. A reasonable agreement is observed at the early stage growth. The deviations that appear at later time could be explained by the fact that our model deals with a compact and homogeneous deposit while atomic force microscopy (AFM) characterizations presented in Fig. 14 show that it is composed of aggregated submicrospheroids. Consequently, light is also scattered by this internal structure and the associated losses, illustrated by the halo observed in the diffraction patterns shown in Fig. 12, were not considered.

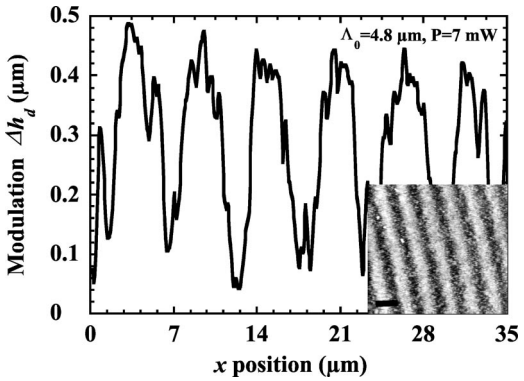

FIG. 14. Atomic force microscopy determination of the stationary relief of a grating photodeposited with an incident beam power $P=7$ mW and a fringe spacing $\Lambda_0=4.8$ μm. The inset presents the associated picture. The bare scale is 5 μm.

To increase accuracy, experiments were thus reiterated over a larger set of beam power. The same values of index contrast, deposit absorption, and normalized reaction rate were found from the fit of whole the runs. We can thus deduce from Eq. (12) the corresponding mean temporal behavior of $\overline{h_d}(t)$ and $\Delta h_d(t)$. As illustrated in Fig. 15, the stationary value of $\Delta h_d(t)$ is in very good agreement with that found from AFM imaging (see Fig. 14) and $\overline{h(t)}_d \gg \Delta h(t)_d$ as already observed in photodeposition of selenium gratings [36,39,40]. Moreover, as expected for a nonlocal coupling (i.e.,$\Phi_C(Q)\sim I(Q)/Q^2$), the background $\overline{h_d}(t)$ is mainly a function of the injected power (this is an intrinsic property of the associated $Q=0$ mode), while the modulation $\Delta h_d(t)$ is extremely sensitive to Λ_0. Finally, using the amplitudes given by the fit, we find that the sine approximation of the logarithmic variation of the profile is justified for $t\ll15\times10^3$ s, which clearly validates our description over the illumination time investigated.

These experiments, as well as the good agreement observed with theory, suggest the way to monitor dynamically the amplitude of the modulation of photodeposited surface relief gratings. Moreover, while we only studied periodic deposition on surfaces driven by two interfering pump beams, the method can easily be extended to multiwave excitation to pattern substrates on demand, as illustrated in Fig. 16.

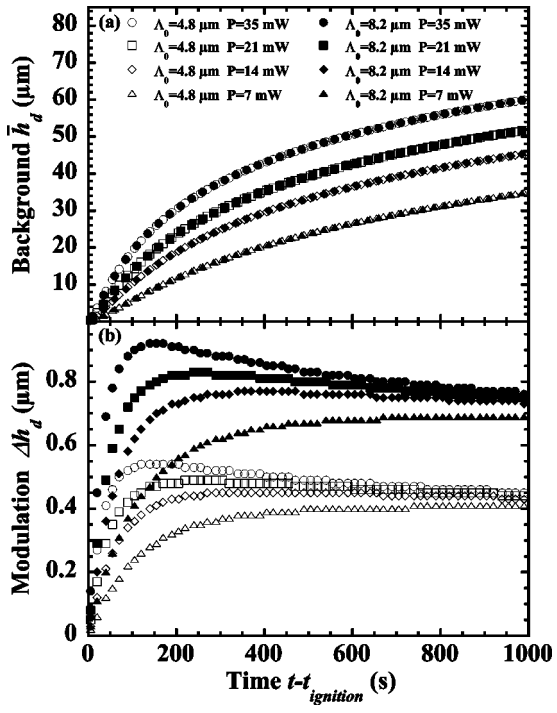

FIG. 15. Dependence on total incident beam power P of the temporal behavior of the pedestal (a) and the modulation (b) heights of photodeposited surface relief gratings deduced from the fit of the measured diffraction efficiencies. To illustrate the influence of the fringe spacing, results are presented for $\Lambda_0=4.8$ μm and $\Lambda_0=8.2$ μm.

C. The ignition time

As illustrated in Fig. 13, photodeposited gratings start to diffract the probe beam after a time delay $t_{ignition}$ that can become significant at low beam power excitation. This effect can be understood from the temporal behavior of the concentration variation in $Cr(OH)_3$ driven by the two interfering pump beams. Indeed, deposition cannot occur before Φ_C reaches solubility Φ_S of $Cr(OH)_3$ on intensity maxima of the fringe pattern. The expression of Φ_C is given by Eq. (23) of Part I for excitation by two interfering pump beams. By neglecting the modulation contribution compared to the background, in agreement with results presented in Fig. 15, the condition $(\Phi_C)_{max} \geqslant \Phi_S$ leads to

$$P \geqslant W^2\left(\frac{\Phi_S D_C}{K^*}\right) \Bigg/ \left[\frac{2}{\sqrt{\pi}} W\sqrt{T} - 1 + \exp(W^2 T)\mathrm{erfc}(W\sqrt{T})\right], \tag{14}$$

where equality corresponds to onset, i.e., $T=T_{ignition}$, and gives the expected variation of $T_{ignition}$ versus P. All the parameters are known from the fitting of the grating efficiencies, except Φ_S. Then, the fit of the set of ignition times measured for the experiments presented above, and illustrated in Fig. 17, leads to $\Phi_S=0.3$. This value, which seems large, is in fact in good agreement with the solubility variation of $Cr(OH)_3$ versus pH [18].

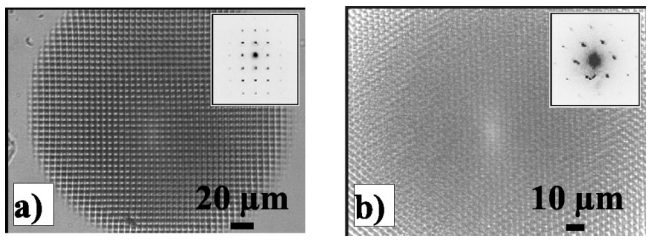

FIG. 16. Surface relief gratings photodeposited using four two-by-two (a) and three 60° oriented (b) interfering pump beams and corresponding diffraction pattern of the probe beam. The incident beam power, the beam waist, the fringe spacing, and the exposition time are, respectively, (a) $P=56$ mW, $a_0=156$ μm, $\Lambda_0=5$ μm, and $t_e=25$ s, (b) $P=50$ mW, $a_0=156$ μm, $\Lambda_0=5$ μm, and $t_e=20$ s.

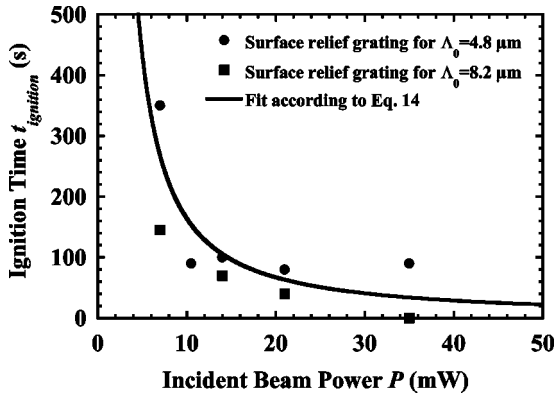

FIG. 17. Dependence on total incident beam power P of the ignition time $t_{ignition}$ required to observe diffraction of the probe beam by photodeposited gratings.

VI. CONCLUSION

We have experimentally explored the kinetics of periodic surface patterning resulting from laser-induced photochemical deposition in liquid solutions. Our goal was to understand the different steps involved in the optical excitation of photosensitive liquid mixtures to form surface relief gratings. Two questions are important here. At first, is it possible to build models that are system-independent—which was the purpose of Part I of this investigation—and are these models sufficiently relevant to experimentally retrieve a majority of the predictions? This second part constitutes the corpus of the present work. Then, if agreement between theory and experiments is good, is it possible to use a model to control *in situ* the dynamics of the desired pattern and to devise its properties? We investigate these two aspects considering the kinetics of surface patterning by the photochemical deposition of chromium oxide layers. All the results were confronted to the model developed in Part I. We have considered the three main ways to build periodic patterns: dot and line arrays, and surface relief modulation deposited by interfering beams. In each case, we analyzed deposit growth as a function of the set of exciting parameters: waist and power of the exciting beam, irradiation time, and scanning velocity or

fringe spacing when relevant. We found good agreement with predictions. In the case of patch deposition under the excitation by a classical Gaussian laser wave, we have seen that its late-stage radial growth is clearly characterized by different scaled laws depending on the ratio between the beam waist and the optical absorption length associated with the mixture. Beyond a simple comparison between theory and experiments, the observed agreement strongly suggests that coarsening theories of first-order phase transitions at late stage can easily be extended to laser-assisted photochemical deposition. We also explored the height growth of the induced deposit in order to check the validity of our spherical cap model to characterize thickness. We showed that this trivial comparison fails for thick deposits, and used an extension of our model that predicts an Elovich's formulation of the height growth. Good agreement with experimental data is found. We then extended our investigation to dynamic line writing by photochemical deposition. While we found reasonable agreement at intermediate beam scanning velocities, our experiments show a significant sensitivity of the deposited lines to this new variable. This analysis clearly deserves further investigation to get a clear cut view of the mechanisms that can disturb line writing, particularly when the rescaled absorption is not totally negligible. Since our analysis is devoted to periodic surface patterning, we also describe experimentally the dynamic building of holographic gratings photodeposited by two interfering pump beams. We showed that the induced relief is composed of a pedestal and a modulation and we characterized quantitatively these two components by analyzing the diffraction pattern kinetics of a probe beam.

As a conclusion, in view of the agreement observed between experiments and predictions, our study shows how the dynamics of photochemical deposition can be devised for applications in periodic patterning. This is of particular interest in material and optical sciences because this agreement suggests that it becomes possible to strongly reduce the number of characterizations when laser excitation or material is changed. A major point in this direction is the observation of scaling regimes. They can be used to predict the properties of the desired patterning and its optical performances whatever the excitation properties are. Due to the role played by photodeposition in surface patterning, lithography, or holography such a universal description furnishes valuable insights to the underlined physics for the design and the control of photodeposited microelements. Experimental extensions to chromium hydroxide deposits in presence of other acids or at different optical wavelengths, as well as deposition of manganese dioxide layers [41], abound in this direction.

[1] D. B. Chrisey, Science **289**, 879 (2000).
[2] M. Hanabusa, Thin Solid Films **218**, 144 (1992).
[3] T. H. Baum and P. B. Comita, Thin Solid Films **218**, 80 (1992).
[4] C. I. H. Ashby, Thin Solid Films **218**, 252 (1992).
[5] J. Malinowski and A. Buroff, Contemp. Phys. **19**, 99 (1978).
[6] Appl. Surf. Sci. **86** (1) (1995), special issue on laser processing, edited by J. Dieleman, U. K. P. Bierman, and P. Hess.
[7] *Laser Microfrabrication: Thin Film Processes and Lithography*, edited by D. J. Ehrlich and J. Y. Tsao (Academic Press, Boston, 1989).
[8] *Laser Processing and Diagnostics*, edited by D. Bäuerle, Springer Series in Chemical Physics Vol. 39 (Springer, Heidelberg, 1984).
[9] D. Bäuerle, *Chemical Processing with Lasers* (Springer, Berlin, 1996).
[10] A. Peled, Lasers Eng. **6**, 41 (1997).
[11] I. Baal-Zedaka, S. Hava, N. Mirchin, R. Margolin, M. Zagon, I. Lapsker, J. Azoulay, and A. Peled, Appl. Surf. Sci. **208/209**, 218 (2003); I. Baal-Zedaka, S. Hava, N. Mirchin, R. Margolin, M. Zagon, I. Lapsker, J. Azoulay, and A. Peled, Colloids Surf., A **217**, 191 (2003).
[12] E. Hugonnot and J. P. Delville Phys. Rev. E **69**, 051605 (2004).
[13] A. J. Bray, Adv. Phys. **43**, 357 (1994).
[14] T. Keinonen and R. Grzymala, Appl. Opt. **38**, 7212 (1999); **38**, 7222 (1999).
[15] G. Manivannan, R. Changkakoti, R. A. Lessard, G. Mailhot, and M. Bolte, J. Phys. Chem. **97**, 7228 (1993).
[16] E. Hugonnot and J. P. Delville (unpublished).
[17] J. R. Waldrop and M. W. Kending, J. Electrochem. Soc. **145**, L11 (1998).
[18] J. P. Jolivet, *De la Solution à l'Oxyde* (CNRS Editions, Paris, 1994).
[19] M. Perakh, A. Peled, and Z. Feit, Thin Solid Films **50**, 273 (1978); M. Perakh and A. Peled, *ibid.* **50**, 283 (1978); **50**, 293 (1978).
[20] J. P. Delville, C. Lalaude, S. Buil, and A. Ducasse, Phys. Rev. E **59**, 5804 (1999); S. Buil, E. Hugonnot, and J. P. Delville, *ibid.* **63**, 041504 (2001).
[21] J. D. Gunton, M. San Miguel, and P. S. Sahni, in *Phase Transitions and Critical Phenomena*, edited by C. Domb and J. L. Lebowitz (Academic, New York, 1983), Vol. 8, p. 269.
[22] A. Peled, A. A. Friesem, and K. Vinokur, Thin Solid Films **218**, 201 (1992).
[23] E. Hugonnot, X. Müller, and J. P. Delville, J. Appl. Phys. **92**, 5520 (2002).
[24] M. Wehner, F. Legewie, B. Theisen, and E. Beyer, Appl. Surf. Sci. **106**, 406 (1996).
[25] M. Ichimura, F. Goto, Y. Ono, and E. Arai, J. Cryst. Growth **198/199**, 308 (1999).
[26] E. Hugonnot, A. Carles, M. H. Delville, P. Panizza, and J. P. Delville, Langmuir **19**, 226 (2003).
[27] M. B. Stern, Microelectron. Eng. **34**, 299 (1997).
[28] L. Petit, J. P. Manaud, C. Mingotaud, S. Ravaine, and E. Duguet, Mater. Lett. **51**, 478 (2001).
[29] A. van Blaarderen, R. Ruel, and P. Wiltzius, Nature (London) **385**, 321 (1997).
[30] V. Weiss, A. A. Friesem, and A. Peled, Thin Solid Films **218**, 193 (1992).

[31] T. H. Baum and C. R. Jones, Appl. Phys. Lett. **47**, 538 (1985).
[32] R. Kullmer, P. Kargl, and D. Bäuerle, Thin Solid Films **218**, 122 (1992).
[33] G. A. Shafeev, Thin Solid Films **218**, 187 (1992).
[34] A. Lachish-Zalait, D. Zbaida, E. Klein, and M. Elbaum, Adv. Funct. Mater. **11**, 218 (2001).
[35] J. R. Salgueiro, V. Moreno, and J. Liñares, Appl. Opt. **41**, 895 (2002).
[36] V. Weiss, A. A. Friesem, and A. Peled, J. Imaging Sci. Technol. **41**, 355 (1997).
[37] E. Hugonnot and J. P. Delville, Appl. Phys. Lett. **80**, 1523 (2002).
[38] H. J. Eichler, *Laser-Induced Dynamic Gratings* (Springer-Verlag, Berlin, 1986).
[39] A. Peled, V. Weiss, D. Rosenblatt, and A. A. Friesem, Opt. Eng. **31**, 70 (1992).
[40] A. Peled, V. Weiss, A. Shalgi, and A. A. Friesem, Appl. Surf. Sci. **79/80**, 393 (1994).
[41] E. Hugonnot and J. P. Delville (unpublished).